

Defect Removal by Solvent Vapor Annealing in Thin Films of Lamellar Diblock Copolymers

Xinpeng Xu,^{*,†,⊥} Xingkun Man,^{*,‡,⊥} Masao Doi,[‡] Zhong-can Ou-Yang,[§] and David Andelman^{||}

[†]Physics Program, Guangdong Technion – Israel Institute of Technology, Shantou, Guangdong 515063, China

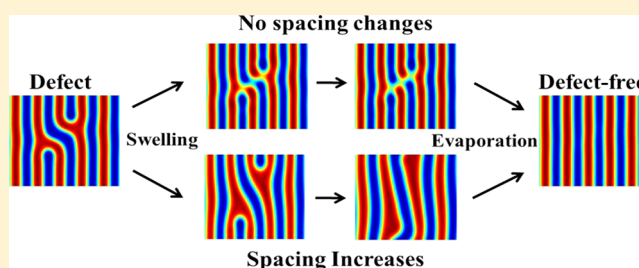
[⊥]Technion - Israel Institute of Technology, Haifa, 32000, Israel

[‡]Center of Soft Matter Physics and Its Applications and School of Physics and Nuclear Energy Engineering, Beihang University, Beijing 100191, China

[§]CAS Key Laboratory of Theoretical Physics, Institute of Theoretical Physics, Chinese Academy of Sciences, Beijing 100190, China

^{||}Raymond and Beverly Sackler School of Physics and Astronomy, Tel Aviv University, Ramat Aviv, 69978 Tel Aviv, Israel

ABSTRACT: Solvent vapor annealing (SVA) is known to be a simple, low-cost, and highly efficient technique to produce defect-free diblock copolymer (BCP) thin films. Not only can the solvent weaken the BCP segmental interactions but it can also vary the characteristic spacing of the BCP microstructures. We carry out systematic theoretical studies on the effect of adding a solvent into lamellar BCP thin films on the defect removal close to the BCP order–disorder transition. We find that the increase of the lamellar spacing, as is induced by addition of the solvent, facilitates more efficient removal of defects. The stability of a particular defect in a lamellar BCP thin film is given in terms of two key controllable parameters: the amount of BCP swelling and the solvent-evaporation rate. Our results highlight the SVA mechanism for obtaining defect-free BCP thin films, as is highly desired in nanolithography and other industrial applications.



The stability of a particular defect in a lamellar BCP thin film is given in terms of two key controllable parameters: the amount of BCP swelling and the solvent-evaporation rate. Our results highlight the SVA mechanism for obtaining defect-free BCP thin films, as is highly desired in nanolithography and other industrial applications.

I. INTRODUCTION

Thin films of a diblock copolymer (BCP) with an extended and defect-free lateral order can serve as ideal templates or scaffolds for fabricating nanoscale functional materials, as is highly desired in nanolithography and ultrafiltration membrane applications.^{1–3} However, when a BCP thin film coats a solid substrate, it is usually kinetically trapped in a nonequilibrium and poorly ordered state with a significant amount of defects, hindering the mainstream use of BCP thin films in nanotechnology.^{1–3} To facilitate the fabrication of defect-free films, further treatments are needed. As examples of techniques that have been developed to tailor the self-assembly behavior of BCP thin films, we mentioned electric field alignment,^{4,5} shear alignment,^{6,7} microwave annealing,⁸ and thermal annealing.^{1,2,9–16} Besides these approaches, solvent vapor annealing (SVA)^{1,3,17–31} has been used to enhance the mobility of polymer chains and to facilitate the annihilation of defects.

In a typical SVA process,^{1,3,19,21,22,29} the BCP thin film is first exposed to vapors of one or more solvents for a certain amount of annealing time. After a swollen and mobile polymer film is formed on the substrate, it is then dried by controlled solvent evaporation. During the film swelling in SVA, solvent molecules diffuse into the thin BCP film and screen (or weaken) the unfavorable interactions between polymer segments, leading to a lower effective Flory–Huggins parameter, χ_{eff} , than its value for dry (no solvent) case.^{21,22,32–34} Hence, the effective Flory–Huggins parameter $\chi_{\text{eff}} = \chi_{\text{eff}}(\phi)$ is a

function of solvent volume fraction, ϕ . Furthermore, as the solvent is introduced, the spacing $\lambda = \lambda(\phi)$ of the microdomains also changes as a function of ϕ .^{3,17–23,29,35,36}

Compared to conventional thermal annealing (TA), SVA offers several unique advantages for defect annihilation:^{1,3,21} (i) SVA provides means to anneal BCPs that are sensitive to thermal degradation. (ii) SVA is generally more effective (with shorter annealing time) in removing defects for thin films of high-molecular-weight BCPs. (iii) SVA provides additional controllable parameters for tuning film morphology. For example, solvent molecules allow the segregation parameterized by $N\chi$ to vary continuously over a larger range than what can be achieved in TA. In addition, selective solvents can be used to induce asymmetric swelling between BCP blocks and thus change the morphology of the BCP film.

Despite the widespread use of SVA, a quantitative understanding of its effect in defect removal has not yet been established.^{1,3,17,21,22,27–31} The two principal problems are lack of standardized SVA processes and no rigorous understanding of the evolution of the nanostructure of the final dried film from its solvent-swollen state. Therefore, it is of interest to investigate theoretically how relevant system parameters affect the BCP swelling and solvent removal in

Received: June 10, 2019

Revised: September 25, 2019

Published: November 26, 2019

SVA.^{22,27,29–31} Such parameters include the swelling ratio (i.e., the fractional increase in the film volume due to solvent absorption), solvent-annealing time, solvent-evaporation rate, film thickness, temperature, and solvent selectivity. The understanding of their effects on the structure of BCP thin films is necessary to fine-tune and control the SVA process to obtain the desired morphology.

Most previous theoretical and computational studies use either self-consistent field theory or particle-based simulation methods that include a large number of molecular parameters.^{27–31} Here, we propose an alternative continuum two-fluid model for SVA processes in BCP thin films. The detailed numerical analysis is carried out employing dimensionless system parameters: (i) Swelling ratio \mathcal{R} , representing the ratio of the swollen film volume V to its original volume V_0 , i.e., $\mathcal{R} \equiv V/V_0$. (ii) Normalized solvent-evaporation rate $\alpha_e \equiv \tau_0/\tau_e$ with τ_e representing the characteristic time for complete solvent evaporation in the swollen film and τ_0 characterizing the time for copolymer reorganization in the scale of microdomain period λ . More specifically, we investigate the removal of a typical defect occurring in symmetric BCP lamellae in their perpendicular orientation by SVA using a nonselective solvent. In SVA experiments of thin BCP films,^{17,21,22} it has been well established that the swelling ratio, \mathcal{R} , and the solvent-evaporation rate, α_e , are the essential annealing parameters and should be specified explicitly. However, a quantitative understanding of their effects on the directed self-assembly using SVA and, particularly, on the efficiency of SVA in defect removal is still missing. Our main theoretical finding is that the lamellar spacing increase induced by the added solvent facilitates a more efficient removal of defects in BCP films. Moreover, the dependence of the final morphology of the dried BCP film on \mathcal{R} and α_e is summarized in a stability diagram, which can be verified in future experiments.

In the next section, we present the thermodynamical modeling of BCP solutions and a two-fluid model for evaporating BCP solution films. A simplified two-dimensional model is obtained in the thin-film limit without macroscopic convection. Our numerical method and the preparation of a specific initial defect are also explained. In Section III, we show and discuss our simulation results. We focus on the effects of the solvent-swelling ratio and solvent-evaporation rate on the removal of the initial defect in the BCP film. This paper is then summarized and concluded in Section IV. Some qualitative remarks are given in the end.

II. MODEL

II.A. Thermodynamics of BCP Solutions: Generalized Landau–Brazovskii Theory. When a BCP melt is exposed to the vapor of a good solvent, solvent molecules diffuse into the melt to form a swollen BCP solution, in which the chains gain mobility. We consider a BCP solution of monodisperse A/B diblocks dissolved in a *neutral* (nonselective) good solvent for which the two polymer–solvent interactions are equal, $\chi_{AS} = \chi_{BS}$. We restrict ourselves to symmetric A/B BCP where an A-block with N_A monomers is covalently bonded to a B-block with N_B monomers such that $N_A = N_B = N/2$ and N being the total chain length (polymerization index). For simplicity, we assume incompressibility upon mixing the solvent and the BCP. In this case, the structure of the BCP solution can be described by two independent order

parameters: the solvent volume fraction ϕ with $0 \leq \phi \leq 1$ and the relative volume fraction of the two blocks

$$\psi \equiv \phi_A - \phi_B \quad (1)$$

with $-1 \leq \psi \leq 1$. In addition, since the BCP solution is incompressible, we have

$$\phi_A + \phi_B + \phi = 1 \quad \text{or} \quad \phi_p + \phi = 1 \quad (2)$$

in which $\phi_p = \phi_A + \phi_B$ is the total volume fraction of A/B copolymer blocks. Another simplifying assumption in the above is that the two monomers have the same molecular volumes.

It has been known that adding a neutral solvent to the BCP melt has a similar effect as increasing the temperature,^{21,23} namely, shifting the phase diagram of BCP melts toward a higher temperature.³⁷ Based on this understanding, a symmetric BCP solution close to the order–disorder transition (ODT) can be described by generalizing the Landau–Brazovskii free energy,^{38–44} \mathcal{F} (in units of $k_B T$) as

$$\mathcal{F}[\psi, \phi] = \int d^3\mathbf{r} \left[f_s(\phi) + \frac{\tau}{2}\psi^2 + \frac{u}{4!}\psi^4 + \frac{\kappa}{2}(\nabla^2\psi + q^2\psi)^2 \right] \quad (3)$$

in which the ideal mixing entropy of the solvent is $f_s(\phi) = \phi \ln \phi - \phi$, and the parameters are given by^{38–43}

$$\tau \simeq 2n_c N(\chi_c - \chi_{\text{eff}}), \quad u \simeq n_c, \quad \kappa \simeq \frac{6n_c}{q^4}, \quad q \sim \frac{1}{R_g} \quad (4)$$

with $n_c = 1/(Na^3)$ being the copolymer closed-packing chain density of an incompressible BCP melt, a the monomer size, $N\chi_c \simeq 10.5$ for the melt ODT (no solvent), $R_g^2 = Na^2/6$ the gyration radius for Gaussian chains, and q is the characteristic wavenumber of ordered BCP microdomains, which gives the thermodynamically preferred lamellar spacing $\lambda = 2\pi/q \sim R_g$.

For a swollen BCP solution with a nonselective solvent, the effective interaction parameter χ_{eff} in τ of eq 4 and the wavenumber q (or the lamellar spacing λ) are both functions of the solvent volume fraction, ϕ . That is, the phase diagram of BCP solutions is described by the same form of energy functional eq 3 as BCP melts, in which the effects of the added solvent are represented by solvent-dependent $\chi_{\text{eff}}(\phi)$ and $q(\phi)$.

For χ_{eff} we follow the experimental results and take the following power-law form^{21,22,32–34}

$$\chi_{\text{eff}} = \chi(\phi_p)^\delta = \chi(1 - \phi)^\delta \quad (5)$$

in which the exponent $\delta > 0$ varies from 1.0 to 1.6 in a wide range of ϕ .^{32–34} This $\chi_{\text{eff}}(\phi_s)$ represents the dilution effect of the added solvent on the polymer chains by reducing the unfavorable A/B segmental interactions. Particularly, the case with $\delta = 1.0$ can be obtained from the mean-field *dilution approximation*,^{32,33} by assuming a uniform distribution of the solvent throughout the BCP structure. The scaling of λ with the volume fraction of the solvent is often approximated by another power law^{3,17–23,29,35,36}

$$\lambda = \lambda_0(\phi_p)^\beta = \lambda_0(1 - \phi)^\beta \quad (6)$$

which represents the effect of the added solvent on the BCP lamellar spacing λ with λ_0 being the lamellar spacing of the dry film. Here, the exponent β can be either positive or negative

and is a characteristic parameter of BCP solutions^{3,17–23,29,35,36} and depends in general on the degree of solvent selectivity, solvent volume fraction, and morphology of the ordered state. Hence, the wavenumber q in the free energy (eq 3) is given by

$$q = q_0(1 - \phi)^{-\beta} \quad (7)$$

with $q_0 \equiv q(\phi = 0) = 2\pi/\lambda_0$.

It is known from previous studies both in BCP bulk solutions^{35,36} and films^{3,21–23} that the solvent-induced changes in lamellar spacing can be classified into two regimes according to the solvent volume fraction, ϕ , with a crossover between them at $\phi = \phi^*$, where ϕ^* is taken in our theory to be an external (material) parameter.

Kinetically controlled regime with $\beta < 0$ for low amount of solvent, $\phi < \phi^*$. Here, the lamellar spacing λ increases with increasing ϕ , and λ is kinetically controlled^{23,35,36} in the sense that the copolymers do not gain much motility. The BCP structure reorganization cannot take place in a typical annealing time, and further addition of the solvent therefore results in an expansion in all directions. For example, it can be obtained from solvent volume conservation that for an isotropic swelling $\beta = -1/3$ and for a uniaxial swelling of a (dense) BCP solution $\beta = -1$.

Thermodynamically controlled regime with $\beta > 0$ for a larger amount of solvent, $\phi > \phi^*$. Here, the lamellar spacing decreases with increasing ϕ . This results from a decrease in the segregation magnitude as seen in eq 5^{3,21–23}. For large ϕ , λ is thermodynamically controlled^{21–23,35,36} in the sense that the copolymers are sufficiently mobile and expand efficiently along the lamellae interface for a given annealing time. Any addition of the solvent can then result in a decrease of the lamellar spacing λ , in a direction *perpendicular* to the interface.

For example, it was found experimentally that $\beta \approx 1/3$ for dilute BCP bulk solutions of polystyrene-polyisoprene (PS-PI) with nonselective solvents^{35,36} and $\beta \approx 2/3$ for dilute solution films of polystyrene-poly(2-vinyl pyridine) (PS-P2VP) with nonselective solvents.^{21,22} The crossover solvent volume fraction, ϕ^* , is found experimentally to be $\phi^* \approx 0.3$ for PS-PI and PS-P2VP copolymers in solutions with a nonselective solvent.^{21,22,35}

The equilibrium structure of a swollen BCP solution is then given by the minimization of the Landau–Brazovskii free energy \mathcal{F} of eq 3 with respect to ψ and ϕ while subject to the constraints of conserved ϕ and phase parameter ψ

$$\mu_s \equiv \frac{\delta \mathcal{F}}{\delta \phi} = \ln \phi = \text{const.} \quad (8)$$

$$\mu_\psi \equiv \frac{\delta \mathcal{F}}{\delta \psi} = \tau(\phi)\psi + u\psi^3 + \kappa \left[q^4(\phi)\psi + 2q^2(\phi)\nabla^2\psi + \nabla^4\psi \right] = \text{const.} \quad (9)$$

Note that in eq 8 we have neglected the ϕ -dependent contribution of τ and q as shown in eqs 4, 5, and 7. This is equivalent to neglecting the influence of copolymers on the chemical equilibrium of a solvent, μ_s ; on the other hand, ϕ appears in eq 9 as τ and q are both functions of ϕ . The resulting equilibrium distribution is consistent with the assumption of uniform distribution of the solvent through the BCP films. In addition, we would like to point out that the Landau–Brazovskii free energy (eq 3) can be further extended to include more physical effects by introducing more terms, e.g., solvent selectivity via a coupling term $\phi\psi$, solvent

accumulation at the A/B interface via a gradient term $(\nabla\phi)^2$, and Marangoni effects via a concentration-dependent rigidity $\kappa(\phi)$.

Finally, the bulk eqs 8 and 9 are supplemented with boundary conditions given at the neutral (nonselective) solid surface by

$$\begin{aligned} \hat{\mathbf{n}} \cdot \nabla \psi &= 0 \\ \hat{\mathbf{n}} \cdot \nabla (\nabla^2 \psi + q^2 \psi) &= 0 \end{aligned} \quad (10)$$

and at the film–air interface

$$\begin{aligned} \nabla^2 \psi + q^2 \psi &= 0 \\ \hat{\mathbf{n}} \cdot \nabla (\nabla^2 \psi + q^2 \psi) &= 0 \end{aligned} \quad (11)$$

Here, $\hat{\mathbf{n}} = (-\nabla_{\parallel} h, 1)/\sqrt{1 + (\nabla_{\parallel} h)^2}$ is the normal unit vector of the film–air interface with h being the film thickness and ∇_{\parallel} being the 2D gradient operator in the xy -plane.

Close to the ODT (where the order–disorder transition occurs), the BCP solution is described by two lengths: the periodic spacing of BCP lamellae $\lambda = 2\pi/q$ and the correlation length $\xi \sim (\tau/\kappa)^{-1/4} \sim \lambda(N\chi_{\text{eff}} - N\chi_c)^{-1/4}$, which diverges at $\chi_{\text{eff}} = \chi_c$ (the ODT). In particular, for BCP solution films below the ODT ($\tau < 0$ or $N\chi_{\text{eff}} > N\chi_c$), a defect-free perpendicular lamellar state can be described in the single-mode approximation (in the limit of weak segregation, $N\chi_{\text{eff}} \geq N\chi_c$) by

$$\psi = \psi_q \cos(qx) \quad (12)$$

with $\psi_q \sim \sqrt{8\tau/u} = 4(N\chi_{\text{eff}} - N\chi_c)^{1/2}$ being the amplitude obtained by minimizing the free energy with respect to ψ_q and $\lambda = 2\pi/q$ being the periodic spacing of the lamellae.

II.B. Dynamics of BCP Solutions: Two-Fluid Model.

With the above-described generalized Landau–Brazovskii free energy, we formulate a two-fluid model for the BCP solutions with a nonselective solvent to explore the dynamic coupling between BCP copolymers and small solvent molecules during SVA. This is in analogy with a two-fluid model used to model polymer solutions, polymer blends, and diblock copolymer melts.^{45–50}

Let us consider a BCP solution in which the bulk flow and diffusion are taking place simultaneously, i.e., the velocities of the A/B blocks differ from each other as well as from the solvent velocity. From the conservation of the solvent and A/B blocks, we have

$$\partial_t \phi_j = -\nabla \cdot (\phi_j \mathbf{v}_j) \quad (13)$$

where $j = A, B$, and S , which represent the three components A-block, B-block, and the solvent, respectively, and \mathbf{v}_j and ϕ_j the velocity and volume fraction of each component, respectively. For simplicity, we assume incompressibility as given in eq 2 and zero volume change upon mixing the solvent in the BCP solution, from which we obtain

$$\nabla \cdot \bar{\mathbf{v}} = 0 \quad (14)$$

with the volume-averaged velocity $\bar{\mathbf{v}}$ defined by $\bar{\mathbf{v}} \equiv \phi_S \mathbf{v}_S + \phi_A \mathbf{v}_A + \phi_B \mathbf{v}_B$.

From eqs 13 and 14, we obtain

$$\begin{aligned} \partial_t \phi + \bar{\mathbf{v}} \cdot \nabla \phi &= -\nabla \cdot \mathbf{j}_S \\ \partial_t \psi + \bar{\mathbf{v}} \cdot \nabla \psi &= -\nabla \cdot \mathbf{j}_\psi \end{aligned} \quad (15)$$

where

$$\begin{aligned}\phi_A &= (1 - \phi + \psi)/2 \\ \phi_B &= (1 - \phi - \psi)/2 \\ \mathbf{j}_S &\equiv \phi(\mathbf{v}_S - \bar{\mathbf{v}}) = -\phi_A(\mathbf{v}_A - \bar{\mathbf{v}}) - \phi_B(\mathbf{v}_B - \bar{\mathbf{v}}) \\ \mathbf{j}_\psi &\equiv \phi_A(\mathbf{v}_A - \bar{\mathbf{v}}) - \phi_B(\mathbf{v}_B - \bar{\mathbf{v}})\end{aligned}\quad (16)$$

where \mathbf{j}_S and \mathbf{j}_ψ are the two currents. Note that ϕ and ψ are both conserved order parameters of the BCP solution.

To determine $\bar{\mathbf{v}}$, \mathbf{j}_S , and \mathbf{j}_ψ we employ Onsager's variational principle,^{45–49,51} in which the Rayleighian functional is $\mathcal{R} = \dot{\mathcal{F}} + \Phi$ with the temporal change rate of free energy given by

$$\partial_t \mathcal{F} = \dot{\mathcal{F}} = \int d^3\mathbf{r} (\mu_\psi \partial_t \psi + \mu_S \partial_t \phi) \quad (17)$$

The dissipation function is generally given by

$$\begin{aligned}\Phi &= \int d^3\mathbf{r} \left[\frac{1}{2} \sum_{ij} \tilde{\zeta}_{ij} \mathbf{v}_i \cdot \mathbf{v}_j + \frac{\zeta_S}{2} (\mathbf{v}_B - \mathbf{v}_S)^2 \right. \\ &\quad \left. + \frac{\eta}{4} (\nabla \bar{\mathbf{v}} + \nabla \bar{\mathbf{v}}^T)^2 \right]\end{aligned}\quad (18)$$

where $i, j = A, B$, and S and the friction matrix $\tilde{\zeta}_{ij}$ must be symmetric. Furthermore, since Φ has to be invariant under the Galilean transformation, we get

$$\sum_i \tilde{\zeta}_{ij} = 0, \quad \sum_j \tilde{\zeta}_{ij} = 0 \quad (19)$$

and hence there are only three independent elements in the $\tilde{\zeta}_{ij}$ matrix. We can now rewrite the Galilean-invariant dissipation function in the form

$$\begin{aligned}\Phi &= \int d^3\mathbf{r} \left[\frac{\zeta}{2} (\mathbf{v}_A - \mathbf{v}_B)^2 + \frac{\zeta_S}{2} (\mathbf{v}_A - \mathbf{v}_S)^2 + \frac{\zeta_S}{2} (\mathbf{v}_B - \mathbf{v}_S)^2 \right. \\ &\quad \left. + \frac{\eta}{4} (\nabla \bar{\mathbf{v}} + \nabla \bar{\mathbf{v}}^T)^2 \right]\end{aligned}\quad (20)$$

or equivalently

$$\begin{aligned}\Phi &= \int d^3\mathbf{r} \left[\frac{1}{2} L_{\psi\psi} \mathbf{j}_\psi^2 + \frac{1}{2} L_{\psi S} \mathbf{j}_\psi \cdot \mathbf{j}_S + \frac{1}{2} L_{S\psi} \mathbf{j}_\psi \cdot \mathbf{j}_S \right. \\ &\quad \left. + \frac{1}{2} L_{SS} \mathbf{j}_S^2 + \frac{\eta}{4} (\nabla \bar{\mathbf{v}} + \nabla \bar{\mathbf{v}}^T)^2 \right]\end{aligned}\quad (21)$$

where the resistance matrix L_{ij} (with $i, j = S, \psi$) is given (up to a prefactor) by

$$\mathbf{L} = \begin{bmatrix} L_{SS} & L_{S\psi} \\ L_{\psi S} & L_{\psi\psi} \end{bmatrix} \quad (22)$$

with

$$\begin{aligned}L_{\psi\psi} &= 4\zeta(1 - \phi)^2 + \zeta_S[(1 - \phi + \psi)^2 + (1 - \phi - \psi)^2] \\ L_{\psi S} &= L_{S\psi} = 4\zeta\psi(1 - \phi) + \frac{\zeta_S}{\phi} \left[(1 - \psi)(1 - \phi + \psi)^2 \right. \\ &\quad \left. - (1 + \psi)(1 - \phi - \psi)^2 \right] \\ L_{SS} &= 4\zeta\psi^2 + \frac{\zeta_S}{\phi^2} \left[(1 - \psi)^2(1 - \phi + \psi)^2 \right. \\ &\quad \left. + (1 + \psi)^2(1 - \phi - \psi)^2 \right]\end{aligned}\quad (23)$$

In the above, we have assumed equilibrium conditions as given in eqs 8 and 9 at the boundaries of the BCP film. The first three terms in the energy dissipation (20)–(21) are caused by the relative motion either between the two polymer blocks or between the polymer blocks and the solvent. The fourth term represents the energy dissipation caused by solvent velocity gradients, where η is the solution viscosity and ζ and ζ_S are the friction constants per unit volume. Note that for neutral solvents (i.e., nonselective solvents that interact equally with A/B blocks), the same friction constant, ζ_S , is used to describe the relative motion between the solvent and the A/B blocks. In addition, we would like to point out that the viscoelastic properties of BCP solutions can be incorporated into the two-fluid model as discussed in ref 46 for polymer solutions and blends.

Substituting eq 15 into eqs 17 and 21, minimizing the Rayleighian with respect to $\bar{\mathbf{v}}$, \mathbf{j}_S , and \mathbf{j}_ψ and substituting the obtained results back into eq 15, we obtain the following set of dynamic equations^{45–49,51}

$$\begin{aligned}\partial_t \phi + \bar{\mathbf{v}} \cdot \nabla \phi &= \nabla \cdot [M_{SS} \nabla \mu_S + M_{S\psi} \nabla \mu_\psi] \\ \partial_t \psi + \bar{\mathbf{v}} \cdot \nabla \psi &= \nabla \cdot [M_{\psi S} \nabla \mu_S + M_{\psi\psi} \nabla \mu_\psi] \\ -\nabla p + \eta \nabla^2 \bar{\mathbf{v}} - \psi \nabla \mu_\psi - \phi \nabla \mu_S &= 0\end{aligned}\quad (24)$$

with the incompressibility condition (14). Here, we have substituted the following constitutive relations resulting from the Rayleighian minimization

$$\begin{aligned}\mathbf{j}_S &= -[M_{SS} \nabla \mu_S + M_{S\psi} \nabla \mu_\psi] \\ \mathbf{j}_\psi &= -[M_{\psi S} \nabla \mu_S + M_{\psi\psi} \nabla \mu_\psi]\end{aligned}\quad (25)$$

into the conservation eq 15. The motility coefficient matrix M_{ij} (with $i, j = S, \psi$) is the inverse of the resistance matrix L_{ij} given in eq 23. It is also symmetric, and its elements in the limit of a dilute solution (i.e., small ϕ) are found (up to a prefactor) to be

$$\mathbf{M} = \begin{bmatrix} \zeta_S^{-1} \phi^2 & -\zeta_{\text{eff}}^{-1} \phi \psi \\ -\zeta_{\text{eff}}^{-1} \phi \psi & \zeta_{\text{eff}}^{-1} \end{bmatrix} \quad (26)$$

where the effective friction constant per volume ζ_{eff} depends on the relative values of ζ and ζ_S .

Note that here, for simplicity, we consider only the case of isotropic diffusion as an application of the two-fluid model. This means that all of the mobility coefficients M_{ij} are scalars.

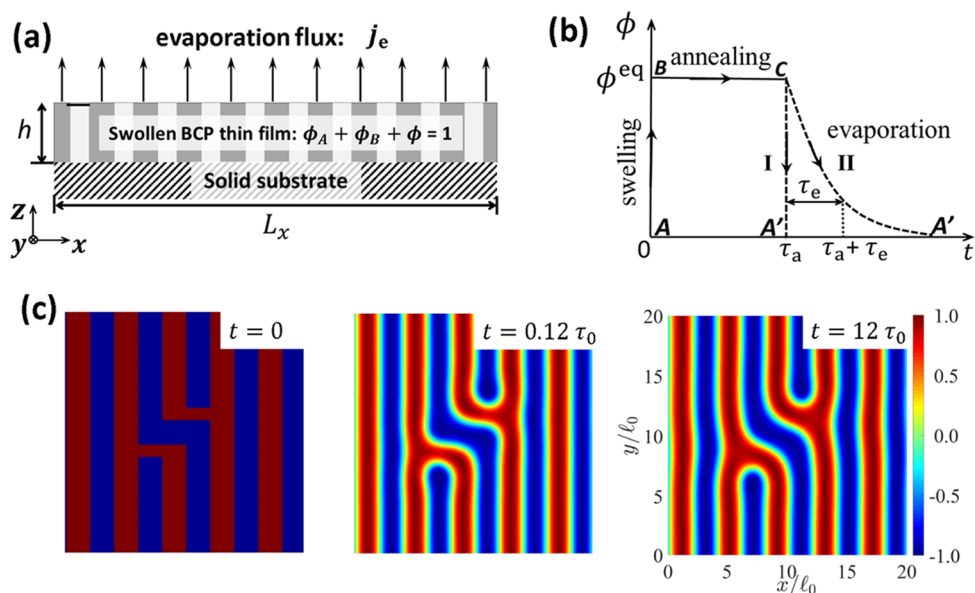


Figure 1. (a) Schematic illustrations of the BCP film setup. (b) Sketch of the temporal evolution of the solvent volume fraction. Three important parameters are shown: the equilibrium solvent volume fraction, ϕ^{eq} , of a swollen film; the annealing time τ_a ; and the characteristic evaporation time τ_e . The lines $A \rightarrow B$, $B \rightarrow C$, and $C \rightarrow A'$ represent the subsequent swelling, annealing, and evaporation (deswelling) processes, respectively. (c) Preparation of the initial metastable defect structure from an artificially prescribed morphology at $t = 0$, and its temporal evolution to $t = 12\tau_0$.

However, it is worthwhile to point out that the copolymer diffusion is in general anisotropic, depending on the BCP morphology.^{29,49,52} Namely, each motility coefficient M_{ij} should be an anisotropic tensorial function of the local morphology. It has been shown that anisotropic diffusion can significantly affect the rate of relaxation of perturbations in BCP films.^{49,52} Particularly, for lamellar BCP films, the effects of transverse mobility are generally negligible as compared to longitudinal copolymer diffusion. Thus, we expect that when a defect becomes unstable, such anisotropic diffusion in a lamellar BCP thin film can significantly increase the longitudinal boundary velocities of defects through the coupling between the longitudinal and transverse diffusive modes within the defect region.

For a thin film of BCP solution, the above set of equations has to be supplemented with proper boundary conditions.⁵¹ At the bottom (neutral) substrate ($z = 0$), we take the no-slip condition for the average velocity and the impermeability conditions for diffusion fluxes as

$$\begin{aligned} \bar{\mathbf{v}} &= 0, \\ \hat{\mathbf{n}} \cdot \mathbf{j}_S &= \hat{\mathbf{n}} \cdot \mathbf{j}_\psi = 0 \end{aligned} \quad (27)$$

with \mathbf{j}_S and \mathbf{j}_ψ given by eq 25 and assume equilibrium conditions for order parameter, ψ , as given in eq 10. At top free surface at $z = h(t)$, we have stress-free conditions

$$\hat{\mathbf{n}} \cdot \boldsymbol{\sigma} = 0 \quad (28)$$

where $\boldsymbol{\sigma} = -\mathbf{p}\mathbf{I} + \eta(\nabla\bar{\mathbf{v}} + \nabla\bar{\mathbf{v}}^T)$ is the viscous stress tensor. We also assume equilibrium conditions for order parameter, ψ , as given in eq 11. In addition, at the free boundary $z = h(t)$, solvent evaporation occurs, and from the evaporation flux defined by $j_e \equiv \rho_0(\bar{\mathbf{v}} - \mathbf{v}_i) \cdot \hat{\mathbf{n}} = \rho_S(\mathbf{v}_S - \mathbf{v}_i) \cdot \hat{\mathbf{n}}$, we can get the kinematic boundary conditions as

$$\begin{aligned} \hat{\mathbf{n}} \cdot \bar{\mathbf{v}} &= \partial_t h + j_e / \rho_0 \\ \hat{\mathbf{n}} \cdot \mathbf{j}_S &= (1 - \phi) j_e / \rho_0 \\ \hat{\mathbf{n}} \cdot \mathbf{j}_\psi &= -\psi j_e / \rho_0 \end{aligned} \quad (29)$$

Here, the velocity of the free film/air interface satisfies $\mathbf{v}_i \cdot \hat{\mathbf{n}} = \partial_t h$. We assume that the evaporation flux follows the Hertz–Knudsen relation^{27,28}

$$j_e = \rho_0 v_e [\phi(h) - \phi^{eq}] \quad (30)$$

in which ϕ^{eq} is the equilibrium solvent fraction of a swollen film in coexistence with the vapor phase and v_e is an adjustable velocity parameter, proportional to the mass transfer coefficient. It relates the rate of evaporative loss τ_e^{-1} from the free surface to the solvent interdiffusion through the film by $v_e = h_0/\tau_e$ with h_0 being the initial thickness of the BCP film. As the surface tension is usually quite small in comparison to the bulk energy of the BCP film, we neglected its contribution. This results in a flat free surface of the BCP film throughout the SVA process.

Regardless of the physical properties of BCP films, the formulated problem is intrinsically nonlinear due to the moving free boundary. Numerical integrations are carried out following a scheme that was successfully employed for other moving boundary problems.^{51,53,54} The method consists of the following four steps: (i) Assume that $\psi(\mathbf{r}, t)$, $\phi(\mathbf{r}, t)$, and $\bar{\mathbf{v}}(\mathbf{r}, t)$ are known functions at time t . The functions $\psi(\mathbf{r}, t)$, $\phi(\mathbf{r}, t)$, and $\bar{\mathbf{v}}(\mathbf{r}, t)$ satisfy eqs 24 and 30. (ii) Neglect the dynamic nature of $\psi(\mathbf{r}, t)$, $\phi(\mathbf{r}, t)$, and $\bar{\mathbf{v}}(\mathbf{r}, t)$. The moving boundary $h(x, y, t)$ is extrapolated to the forward time step, $t + \Delta t$, by means of an explicit forward difference expression of eq 29 (iii) Let the boundary $h(x, y, t)$ be fixed at the new time step $t + \Delta t$. Determine $\psi(\mathbf{r}, t + \Delta t)$, $\phi(\mathbf{r}, t + \Delta t)$, and $\bar{\mathbf{v}}(\mathbf{r}, t + \Delta t)$ of the forward time step satisfying eq 24 and the boundary conditions 27 through eq 30. (iv) Repeat the iteration scheme of the previous second and third steps till a final time, t_{final} .

II.C. Two-Dimensional Model for Thin BCP Films. We consider the limit of no macroscopic convection^{46,47} and focus on thin films of concentrated BCP solutions (with relatively small ϕ). Then, from eq 26, we have $M_{S\psi} = M_{\psi S} \approx 0$. That is, the cross-coupling between the solvent and copolymer dynamics can be neglected. In this case, the above set of eqs 24–28 and 30 reduces to^{55,56}

$$\begin{aligned}\partial_t \phi &= -\nabla \cdot \mathbf{j}_S, & \mathbf{j}_S &= -M_{SS} \nabla \mu_S \\ \partial_t \psi &= -\nabla \cdot \mathbf{j}_\psi, & \mathbf{j}_\psi &= -M_{\psi\psi} \nabla \mu_\psi\end{aligned}\quad (31)$$

supplemented with boundary conditions at the bottom substrate, $z = 0$

$$\begin{aligned}\hat{\mathbf{z}} \cdot \mathbf{j}_S &= \hat{\mathbf{z}} \cdot \mathbf{j}_\psi = 0 \\ \partial_z \psi &= 0 \\ \partial_z (\nabla^2 \psi + q^2 \psi) &= 0\end{aligned}\quad (32)$$

and at the top free surface, $z = h(t)$

$$\begin{aligned}\hat{\mathbf{z}} \cdot \mathbf{j}_S &= (1 - \phi) j_e / \rho_0 \\ \hat{\mathbf{z}} \cdot \mathbf{j}_\psi &= -\psi j_e / \rho_0 \\ \nabla^2 \psi + q^2 \psi &= 0 \\ \partial_z (\nabla^2 \psi + q^2 \psi) &= 0\end{aligned}\quad (33)$$

with the evaporation flux given by eq 30. For a small volume fraction of the solvent with $\mu_S \approx 2A_2\phi$ and A_2 being the second virial coefficient, the dynamic equation for the solvent in eq 31 reduces to a simple diffusion equation with the collective diffusion constant given by $D_S = 2A_2M_{SS} \sim 2A_2\zeta_S^{-1}\phi^2$.

Furthermore, we take the limit that the relaxation dynamics throughout the film thickness (z -direction) is much faster than the lateral one (xy -plane), as is schematically shown in Figure 1a. The variations of ψ and ϕ are then negligible in the normal direction (z -axis), leading to $\psi = \psi(x, y, t)$ and $\phi = \phi(t)$, and the changes of BCP morphology occur in the two-dimensional xy -plane. The solvent volume fraction ϕ is a spatially uniform “external” control parameter, which is determined by the evaporation rate of the solvent at the free surface.

In the simplified limit, the temporal evolution of the phase structure is determined by the following 2D Cahn–Hilliard equation^{55,56}

$$\partial_t \psi = \nabla_{\parallel} \cdot (M_{\psi\psi} \nabla_{\parallel} \mu_\psi) \quad (34)$$

in which ∇_{\parallel} denotes the 2D spatial gradient in the xy -plane. Moreover, from eqs 31 to 34, we obtain the temporal evolution of the film thickness and the integrated solvent fraction, respectively, as

$$\partial_t h + j_e / \rho_0 = 0 \quad (35)$$

$$\partial_t (h\phi) + j_e / \rho_0 = 0 \quad (36)$$

from which we derive

$$\begin{aligned}h &= h_0 / (1 - \phi) \\ \partial_t \phi &= -\tau_e^{-1} (1 - \phi)^2 (\phi - \phi^{eq})\end{aligned}\quad (37)$$

That is, the morphological dynamics of thin BCP film in the xy -plane is described by eq 34 for the order parameter ψ ,

which, in turn, is controlled by the solvent fraction ϕ following eq 37.

Finally, we would like to point out that the above limit is justified when the viscous time scale $\tau_v = h_0^2/\nu$ (with ν being the kinematic viscosity of the BCP solution) is much smaller than the evaporative time $\tau_e = h_0/v_e$ for an initially stationary film to evaporate to a dry film, i.e., $\tau_v \ll \tau_e$. Furthermore, we focus on the simple case that the evaporation of the solvent is slow compared with the vertical solvent/polymer diffusion, i.e., $\tau_e \gg \tau_S, \tau_P$, with $\tau_S = h_0^2/D_S$ and $\tau_P = h_0^2/D_P$ being the diffusion times through the film thickness of the solvent and the polymer segments, respectively, and D_S and D_P the corresponding collective diffusion constants.

II.D. Numerical Method and System Setup. Using the classical central finite-difference method,^{48,57} we numerically integrate the dynamical eq 34 for the order parameter ψ and eq 37 for ϕ (in the xy -plane), as is schematically shown in Figure 1a. The length is measured in units of

$$l_0 \equiv (\kappa/u)^{1/4} \quad (38)$$

and from eq 4, we obtain $l_0 \approx 0.25\lambda_0$. Note that the number of lamellar periods in our simulation box equals to an integer that is the closest to L_x/λ_0 . It is five for $L_x = 20l_0$ and dry lamellar spacing $\lambda_0 \approx 4l_0$, as can be seen in Figure 1c.

Time is measured in units of

$$\tau_0 \equiv l_0^2/uM_{\psi\psi} \quad (39)$$

which characterizes the time for copolymer reorganization in the scale of the lamellar period $\lambda_0 \sim l_0$.

We employ periodic boundary conditions in the simulations to realistically model experimental setups of BCP films. The experimental lateral size is extremely large and cannot be modeled in any finite simulation box. However, periodic boundary conditions are the best way to model large systems as any effect of an artificially imposed lateral wall is removed. The box lateral size is set to include an integer number of lamellae to remove the artificial confinement effect that does not exist in the experiments. In addition, we have also varied the time step and mesh size to confirm the accuracy and efficiency of our numerical scheme. For a mesh size of $0.05l_0$, the simulations are stable for time steps smaller than $5 \times 10^{-8}\tau_0$, whereas for meshes of size $0.4l_0$, the simulations are stable for time steps smaller than $5 \times 10^{-7}\tau_0$. We note that the results are not found to be sensitive to the mesh size and time step in the tested range. Specifically, in most of the presented simulations (except for Figures 4 and 6), we have chosen the mesh size to be $0.1l_0$ and the time step $10^{-8}\tau_0$ for a simulation box size of $L_x = L_y = 20l_0$.

We carry out a numerical study for the effects of solvent swelling and solvent evaporation on the morphology of a dry BCP film with a specific defect as shown in Figure 1c. In our simulations, the initial defective morphology of the dry film is prepared at $N\chi = 30$, starting from an artificially designed initial morphology that is close to the desired defect structure as shown in Figure 1c. In addition, when the dry film is exposed to solvent in experiments, the uptake (swelling) rate of the solvent in most cases strongly depends on the morphology of BCP films even for a nonselective solvent.¹⁹ However, the exposure time to solvent vapor (the annealing time) is usually longer than that required for the film to swell and reach an equilibrium (solvent) volume fraction.^{19,21} In our

simulations, we ignore the effect of the solvent uptake process and assume “instantaneous” saturation to equilibrium (solvent) volume fraction ϕ^{eq} as schematically shown in Figure 1b. After an annealing time τ_a , the solvent is removed by a controlled evaporation rate, $1/\tau_e$, according to eq 37.

III. RESULTS AND DISCUSSION

We present results on the effects of two key parameters on defect removal during SVA: solvent-swelling ratio \mathcal{R} , which is a monotonic function of equilibrium volume fraction ϕ^{eq} , and the normalized solvent-evaporation rate, $\alpha_e = \tau_0/\tau_e$.

III.A. Effects of the Solvent-Swelling Ratio. The swelling of the BCP film is one-dimensional along the normal z -direction, due to the lateral confinement of the fixed area set by the in-plane periodic boundary conditions, as shown in Figure 1a. The swelling ratio $\mathcal{R} \equiv V/V_0$ is then given by

$$\mathcal{R} = h/h_0 = \frac{1}{1 - \phi^{\text{eq}}} \quad (40)$$

from the conservation of copolymers and eq 37 with h_0 and h being the film thicknesses of the original dry film and the swollen film, respectively.

III.A.1. Negligible Changes in the Lamellar Spacing with $\beta = 0$. As pointed out in Section II, there are two major effects of a nonselective solvent that swells a BCP film: dilution effect acting on $\chi_{\text{eff}}(\phi)$, eq 5, and increase of the lamellar spacing $\lambda(\phi)$, eq 6. We first concentrate on a simpler case for which the solvent-induced change in the lamellar spacing, λ , is negligible during solvent annealing. Hence, $\lambda \approx \text{const}$. This is modeled by the limit $\beta \approx 0$ in eq 6. It can result from the weak dependence of either χ_{eff} on ϕ or λ on the incompatibility $N\chi_{\text{eff}}$.^{21,22}

From the simulations, we can infer that the defect stability strongly depends on ϕ^{eq} (or swelling ratio \mathcal{R} given in eq 40) in the swollen film. For a relatively small \mathcal{R} (small ϕ^{eq}), the system is kinetically trapped (metastable). On the other hand, in the limit of a very large swelling ratio, occurring for $\chi_{\text{eff}} < \chi_c$ (equivalently, for $\mathcal{R} > 2.86$ or $\phi^{\text{eq}} > 0.65$), the BCP undergoes an order–disorder transition (ODT) and the BCP solution evolves into a disordered phase (no lamellar phase). As shown in Figure 2, only in a narrow window of swelling ratio, $2.5 < \mathcal{R} < 2.86$ (or equivalently $0.6 < \phi^{\text{eq}} < 0.65$), the copolymer

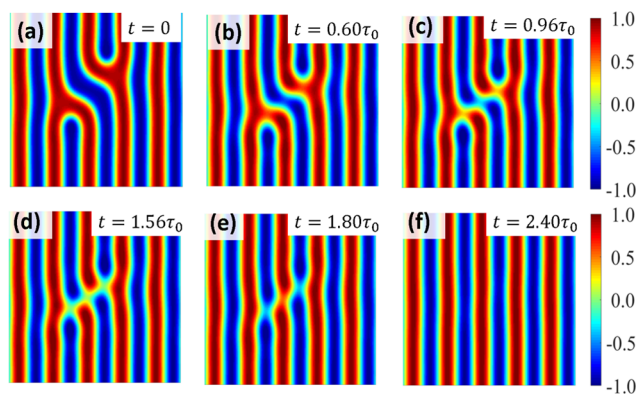


Figure 2. Defect removal upon instantaneous solvent swelling for $\beta = 0$ leading to $\lambda = \text{const}$. only due to the dilution effect on the $\chi_{\text{eff}}(\phi)$ parameter, given the term $\chi(1 - \phi)$ in eq 5. Other parameters are $N\chi = 30$ and $\phi^{\text{eq}} = 0.6$, which corresponds to a swelling ratio of $\mathcal{R} = 2.5$.

segments gain large enough mobility and maintain an ordered structure such that a defect-free lamellar structure is obtained. Note that this window in \mathcal{R} values should be considered only for the case of very long annealing times and very slow solvent evaporation. In other cases, it can be varied significantly by changing the solvent-evaporation rate, α_e , as shown in the inset of Figure 7.

The mechanism of defect removal by the added solvent (reducing χ) is very similar to thermal annealing (TA), where $\chi \sim 1/T$.^{2,9,10,12,13} The presence of a threshold value of incompatibility in $N\chi_{\text{eff}}$ (given by a threshold of ϕ or \mathcal{R}) in SVA has also been seen in TA,^{2,9–14} where $N\chi$ is a function of T . For small $N\chi_{\text{eff}}$ (large swelling ratio), defects are unstable and can be removed spontaneously as there are no energy barriers to overcome. For large $N\chi_{\text{eff}}$ (small swelling ratio), defects are metastable and some free-energy barriers need to be overcome. However, in the simulation method, the morphology dynamics is driven by free-energy minimization. Therefore, we can neither examine the stability of a metastable defect nor quantify the dependence of the energy barrier on $N\chi_{\text{eff}}$ or ϕ . We can only check when the energy barrier of the defect removal vanishes and the defect becomes unstable as \mathcal{R} is increased (see discussions above), as well as examine the dynamic processes of spontaneous defect removal.

Such dynamic processes have a symmetric pathway in the sense that the two horizontal arms break simultaneously, as seen in Figure 2a. This is in contrast to the kinetic pathway of defect removal that is seen in TA studies. Here, the defect removal pathway is asymmetric⁹ in the sense that the two defect horizontal arms (shown in Figure 1c) break sequentially, one after the other, by crossing two consecutive free-energy barriers.^{11,13,14}

III.A.2. Solvent-Induced Increase in the Lamellar Spacing with $\beta < 0$. We also find on general grounds that the change in the lamellar spacing λ during solvent annealing of BCP films is visible and cannot be neglected.^{3,21,23} At small ϕ^{eq} below some critical value, ϕ^* ,^{35,36} the spacing λ increases with increasing ϕ . In Figure 3, we take $\phi^{\text{eq}} = 0.4$, which is smaller than ϕ^* . Also, for $\beta < 0$, the equilibrium lamellar spacing increases from $\lambda_0 \approx 4l_0$ for the dry state to $\lambda \approx 6l_0$ for the swollen state. Correspondingly, the energy-preferred number of lamellar periods, given by L_x/λ_0 , changes from five to three. Figure 3 shows that an increase in lamellar spacing tends to drive long-wavelength structural evolution. After the defect removal is completed, the system evolves into an intermediate metastable defect-free state with four lamellar periods instead of energy-preferred three periods. This result again indicates that the addition of the solvent alters the kinetic pathway of the microstructure evolution of the BCP film.

Comparing the results obtained with spacing changes ($\lambda \neq \text{const}$) as in Figures 3 and 4 to those without spacing changes ($\lambda = \text{const}$. as in Figure 2), we find that in both cases the defect-free state can be obtained only in a narrow window of ϕ . This observation is large enough to make the defect state unstable as well as it exists below ODT to be in the ordered lamellar phase. This observation agrees with experiments.¹⁷ Even more interesting is the fact that the defect structure of a BCP solution with $\phi^{\text{eq}} = 0.4$ is still metastable in the latter case without changes in λ . However, the domain becomes unstable in the former case with an increase in spacing (as shown in Figure 3). We, therefore, assert that the solvent-induced increase in $\lambda(\phi)$ facilitates a more efficient removal of defects. It seems reasonable to conjecture at this point that this

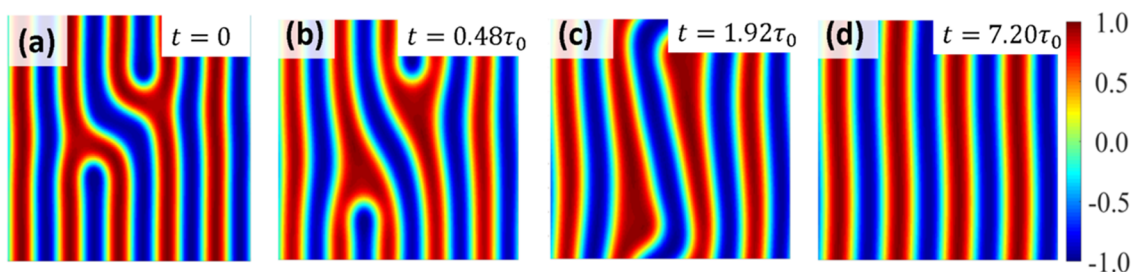


Figure 3. Destabilization of defects upon instantaneous solvent swelling due to an increase in the lamellar spacing. Here, we take $N\chi = 30$, $\phi^{\text{eq}} = 0.4$ (corresponding to $\mathcal{R} \approx 1.67$) and $\beta = -1.0$ as defined in eq 6.

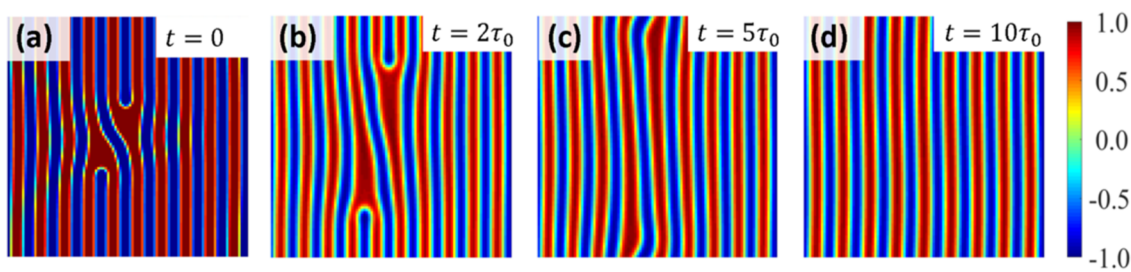


Figure 4. Defect removal in a film with larger lateral dimensions, $L_x = L_y = 40l_0$. The mesh size is $0.4l_0$, and the time step is $10^{-7}\tau_0$. All other parameter values are the same as in Figure 3.

important observation is more general than the specific model we have presented in this study.

III.A.3. Effects of the System Size for $\beta < 0$. The lateral confinement set by periodic boundary conditions also plays a role in determining the final morphology of the thin film. We have carried out larger-scale simulations as shown in Figure 4, where the system sizes are doubled in both lateral directions (see Figure 3). Comparing these results in Figure 4 with those in Figure 3, we find that for larger systems, it takes longer times to remove the defect because the distance of the defect from the boundary is larger. However, the dynamics of defect removal is qualitatively similar for the two different system sizes. In both cases, the defects are unstable and move along the lamellae when the same fraction of the solvent is added.

III.B. Effects of the Solvent-Evaporation Rate. It is well known that the final morphology of the dried BCP film depends not only on the swelling ratio \mathcal{R} but also on the solvent-evaporation rate, α_e .^{3,19,21,23} To examine this dependence, we carry out simulations for swollen films with different swelling ratios \mathcal{R} (i.e., with different ϕ^{eq}) for evaporation at different α_e rates. As schematically shown in Figure 1b, the solvent is removed by evaporation following eq 37 after annealing time, τ_a .

III.B.1. Dependence of the Dried BCP Film Morphology on α_e at Different \mathcal{R} . For a small swelling ratio $\mathcal{R} < 1.2$ ($\phi^{\text{eq}} < 0.15$), the amount of the solvent in the swollen film is not sufficient to enhance polymer chain mobility and the original defect remains metastable and kinetically trapped. After solvent evaporation, the original defect persists in the dried film and is found to be independent of the evaporation rate.

In contrast, at a large swelling ratio $\mathcal{R} > 2.86$ ($\phi^{\text{eq}} > 0.65$) where $N\chi_{\text{eff}} < N\chi_c$, the system passes through the ODT and the swollen BCP film is disordered. After the solvent evaporates, the film re-enters into the ordered phase, but the final dry film is usually trapped in a poorly ordered state characterized by a significant amount of defects. Furthermore, the final phase morphology strongly depends on the evaporation rate. To

obtain a defect-free state, one has to direct the film morphology by controlling the solvent-evaporation rate^{26–28} or by applying a shear flow.^{6,7}

At intermediate swelling ratio $\mathcal{R} \sim 1.7$ ($\phi^{\text{eq}} \sim 0.4$), the copolymer chains have sufficient mobility and the defect is removed spontaneously if the annealing time τ_a is long enough, as shown in Figure 3. In SVA experiments, the solvent evaporates after some small annealing time, $\tau_a < \tau_0$. This motivated us to choose an annealing time $\tau_a = 0.48\tau_0$, after which the solvent is evaporated with the controlled rate, τ_e^{-1} .

III.B.2. Quantifying the Defect Strength of the BCP Film at Different α_e . To quantify how the evaporation rate influences the defect dynamics, we introduce for convenience a new parameter defined as $\Psi \equiv \sum_{ij} (\psi_{ij} - \psi_{i,1})^2$, with i, j denoting the sites in the computational box. Although this “defect strength” parameter is not uniquely defined for a particular morphology, and even is not meaningful if tilting of the lamellae occurs, it is simpler to analyze Ψ than to look directly at the specific film morphology. From the temporal evolution of this parameter shown in Figure 5, we can quickly see that the phase structure of the dried BCP film strongly depends on the evaporation rate $\alpha_e = \tau_0/\tau_e$. The initial defect [Figure 5(a)] can be removed only via slow evaporation with $\alpha_e \ll 1$, as in Figure 5(c1) [a snapshot before the defect is removed can be seen in Figure 5(b1)]. At intermediate evaporation rates with $\alpha_e \sim 1$, the initial defect becomes unstable but is retrapped into another defective structure (but with larger spacing) as shown in Figure 5(c2), whereas at fast evaporation, $\alpha_e \gg 1$, the defect persists as shown in Figure 5(c3).

It is interesting to note that in the simulations, we have not seen any annihilation of the new intermediate defect [Figure 5(c2)] up to times $\sim 620\tau_0$. However, such a defect has been found in previous self-consistent field simulations¹² to be thermodynamically unstable but with very long annihilation times. The understanding of this inconsistency deserves further studies, although these will be difficult to perform using our

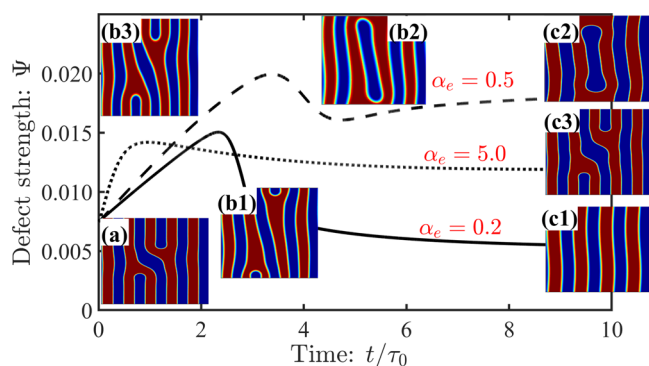


Figure 5. Temporal evolution of the defect structure (shown in Figure 1c) of a swollen BCP film at various evaporation rates $\alpha_e = 0.2$, 0.5 , and 5.0 after annealing time $\tau_a = 0.48\tau_0$. The Flory parameter is $N\chi = 30$, $\phi^{eq} = 0.4$, corresponding to $\mathcal{R} \approx 1.67$ and $\beta = -1.0$ as in eq 6. The defect strength is defined by $\Psi \equiv \sum_{i,j} (\psi_{ij} - \psi_{i,1})^2$, with i, j denoting the sites, and is a convenient way to quantify the process of defect removal in the computational box. Snapshots of the temporal evolution of the original defect (a) (no solvent) are shown for different evaporation rates, α_e . For slow evaporation, the defect (a) is removed and the system evolves spontaneously toward a defect-free state (c1), after crossing an intermediate transition state (b1). In contrast, for faster evaporation, the defect (a) is either kinetically trapped as in state (c3) after crossing the intermediate transition state (b3) or becomes unstable and is retrapped in a new defect state (c2) after crossing (b2).

method. Other methods such as the string method can be used in future studies to explore the energy landscape.

III.B.3. Influence of the Finite System Size. To investigate the influence of the finite system size on the evaporation rate results (Figure 5), we have carried out larger-scale simulations and present them in Figure 6. The system size is doubled in both lateral directions, and the simulations are applied to the specific case presented in Figure 5(c2) with evaporation rate $\alpha_e = 0.5$. Comparing these results, we find that for larger systems, it takes a longer time for the defect to be removed as can be seen in Figure 4 because of the larger distance of the defect from the boundary. However, the dynamics of the defect removal remains qualitatively similar. For an intermediate solvent-evaporation rate ($\alpha_e = 0.5$), the initial defect becomes unstable and the thin film is retrapped into a new intermediate defect state, as shown in Figures 5(c2) and 6.

III.B.4. Morphology of the Dried Film Emerging from the Competitions in Multiple Time Scales. All of these results can be understood in terms of the total sum of annealing time τ_a and the evaporation time τ_e . The combined $\tau_a + \tau_e$ gives the time allowing the copolymers to reorganize during SVA (with characteristic time τ_0). For a given small τ_a , when the solvent is

removed rapidly, the copolymer loses its mobility almost instantly and is kinetically trapped into the defect-swollen morphology. When the solvent is removed gradually, on the other hand, the lamellar spacing changes and the defects are destabilized. Moreover, the BCP microdomains have time to relax so that the defects can be removed, just as in the case of very long annealing times without solvent evaporation. In the annealing process of thin BCP films on neutral substrates by nonselective solvents, the most efficient pathway to remove defects is first to swell the BCP film sufficiently such that defects become unstable and only then to evaporate the solvent rapidly when the defect is almost “healed” spontaneously.

III.B.5. Defect Stability Diagram Showing the Dependence of the Dried Film Morphology on \mathcal{R} and α_e . Finally, we note that the dependence of the final morphology of dried BCP films on the solvent-swelling ratio \mathcal{R} and the solvent-evaporation rate α_e can be summarized in a defect stability diagram, as shown in Figure 7. Three regions are identified:

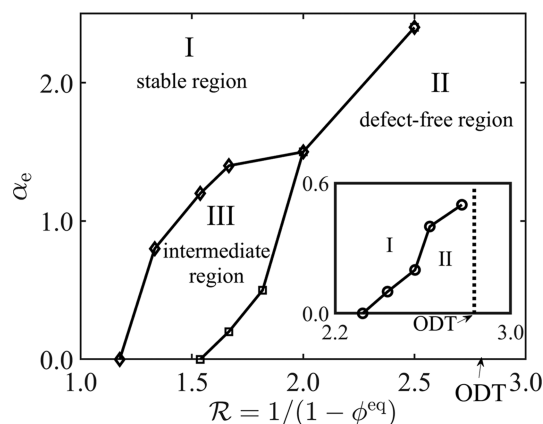


Figure 7. Defect stability diagram shown in Figure 1c during SVA due to the dilution effect and changes in the lamellar spacing. The diagram is plotted in terms of two parameters: the swelling ratio $\mathcal{R} = 1/(1 - \phi^{eq})$ and the evaporation rate $\alpha_e = \tau_0/\tau_e$. We set $N\chi = 30$ and the solvent-induced spacing exponent $\beta = -1.0$ as in eq 6. The solvent is evaporated after an annealing time $\tau_a = 0.48\tau_0$. Three regions are identified: *stable region* (I), where the original defect is still (meta-) stable; *defect-free region* (II), where the defect becomes unstable and is removed spontaneously; *intermediate region* (III), where the original defect is unstable but is retrapped into a new defect state. The lines are shown to guide the eyes. (Inset) The same defect stability diagram but with $\lambda = \text{const.}$ (no spacing changes are allowed) during SVA.

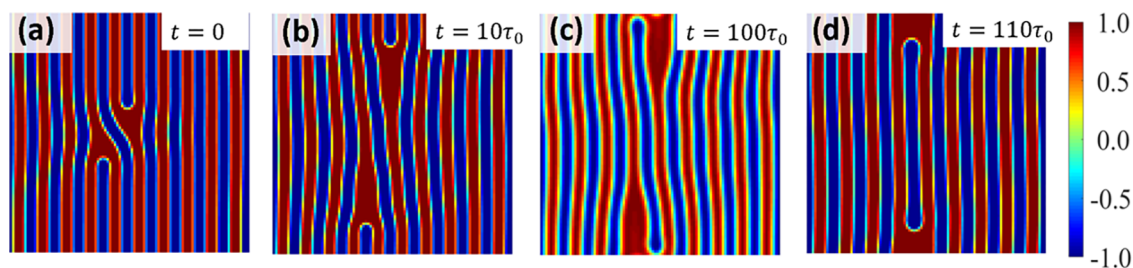


Figure 6. Defect destabilization and its retrapping into an intermediate defect state in a film with larger lateral dimensions of $L_x = L_y = 40l_0$. The mesh size is $0.4l_0$, and the time step is $10^{-7}\tau_0$. All other parameters are the same as in Figure 5(b2) and (c2) with the evaporation rate $\alpha_e = 0.5$.

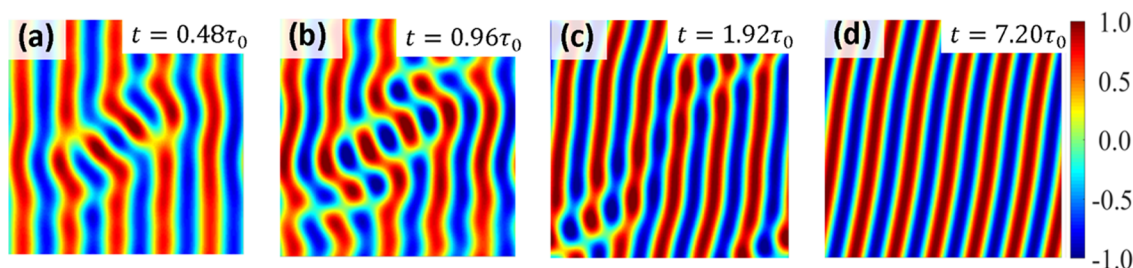


Figure 8. Destabilization of defects upon instantaneous solvent swelling due to the changes in the lamellar spacing λ . The used parameters are $N\chi = 30$, $\phi^{\text{eq}} = 0.6$, and $\phi^* = 0.1$. As ϕ increases, λ increases (with an exponent $\beta = -1.0$) when $\phi < \phi^*$ but decreases (with $\beta = 1/3$) when $\phi > \phi^*$.

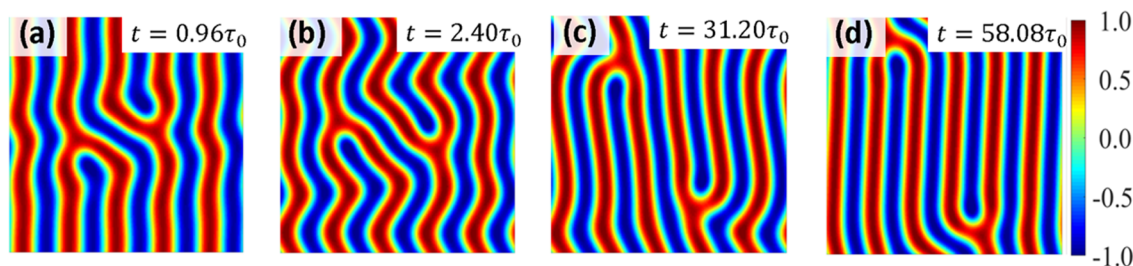


Figure 9. Destabilization of defects upon instantaneous solvent swelling due to the change of the lamellar spacing λ . The used parameters are $N\chi = 30$, $\phi^{\text{eq}} = 0.4$, and $\beta = 1/3$, as defined in eq 6.

(I) A *stable region* at small \mathcal{R} and large α_c , in which the original defect is still stable or metastable and persists in the dried film; (II) a *defect-free region* at large \mathcal{R} and small α_c , in which the defect becomes unstable and is removed spontaneously; (III) an *intermediate region*, in which the original defect is unstable but can be retrapped into a new defect state. Such trapping or transition into an imperfect lamellar structure with a new defect has been reported previously. Using the TA technique, in-plane defect pairs^{11–13} and cross-sectional out-of-plane defect pairs¹⁴ have been observed.

When the solvent-induced changes in lamellar spacing, λ , are negligible (see the inset of Figure 7 where $\lambda = \text{const.}$), the stability diagram contains only two regions: (I) a stable-defect region and (II) a defect-free region. Note that the intermediate region (III) does not exist anymore. Moreover, the defect-free region (II) is much smaller when the solvent-induced spacing changes are taken into account. Another remark is that the numerical accuracy of the stability diagram depends on the choice of the mesh size. Only a small enough mesh size can fully resolve the “shape” of the free-energy landscape and gives accurate stability. Here, we have chosen the mesh size to be $0.1l_0$ as defined in eq 38 and checked that it gives the same diagram as with a smaller mesh size twice as small, $0.05l_0$. Furthermore, the defect stability also depends on the ratio of the lamellar spacing between the swollen state and the dry state, \mathcal{R} , and the exponent β defined in eq 6, as will be discussed in the next section. Our computational prediction agrees, at least qualitatively, with experimental observations^{21,22} and indicates that the two key parameters \mathcal{R} and α_c not only affect the lamellar spacing of BCPs but also govern the removal of defects and lateral ordering of the BCP microdomains. However, the predicted stability diagram still needs to be verified quantitatively in future experiments and more extended simulations.

III.C. Effects of the Spacing Decrease Induced by Large ϕ . As discussed in Section II.A, the effect of the added solvent on the lamellar spacing can be divided into two regimes, separated by a crossover solvent volume fraction, ϕ^* .

In previous sections, we have taken ϕ^* to be large such that $\phi < \phi^*$ and the lamellar spacing increases with the added solvent. Here, we choose small ϕ^* and explore the effect of spacing changes in the two regimes and concentrate, in particular, on the effect that increasing ϕ has on decreasing λ .

In both regimes, $\phi > \phi^*$ and $\phi < \phi^*$, we find that the change in lamellar spacing, λ , destabilizes the defect, as shown in Figures 8 and 9. However, the kinetics of defect instability is very different in the two regimes. At small $\phi < \phi^*$, the solvent-induced λ increases and tends to drive long-wavelength structural evolution, as shown in Figure 3. Moreover, the kinetically controlled spacing increase (when $\phi < \phi^*$) during solvent annealing is essential for removing BCP defects efficiently, as shown in Figure 8. In contrast, at large $\phi > \phi^*$, the solvent-induced λ decreases and introduces small-wavelength undulations, as shown in Figure 9. Note that the obtained defect-free lamellae adopt a tilted orientation in the xy -plane to adjust to the smaller domain size under the constraints imposed by a fixed $L_x \times L_y$ size of the simulation box.

We find that the solvent-induced λ decrease at large ϕ induces small-wavelength undulations in contrast to the long-wavelength structural evolution, as shown in Figure 3. However, these small-wavelength undulations are usually not enough to remove defects as shown in Figure 9. Efficient defect removal occurs only for cases with a significant spacing increase during solvent annealing at small $\phi < \phi^*$.

IV. CONCLUSIONS

We have constructed a two-fluid model to study the microphase separation dynamics of block copolymer (BCP) thin films and applied it to solvent vapor annealing (SVA) processes. We focus on the effect of the added (nonselective) solvent on the defect annihilation in ordered BCP thin films on neutral substrates. More specifically, we investigate the solvent-facilitated removal of a single defect occurring in symmetric lamellar BCP thin films with lamellae perpendicular to the substrate.

In our phenomenological two-fluid model, we have included two key features of the added solvent: weakening the unfavorable interactions between polymer segments and changing the characteristic spacing of the BCP lamellae. We find that the solvent-induced increase of the lamellar spacing in a dense polymer solution (namely, at small solvent volume fraction, ϕ) facilitates an efficient removal of defects. The kinetic pathway of defect removal during SVA is quite different from that of thermal annealing (TA) and depends sensitively on the volume fraction, ϕ , and on the dynamics of the added solvent. The final morphology of the dried BCP film after the SVA process depends not only on solvent-swelling ratio \mathcal{R} (or solvent volume fraction, ϕ) but also on the solvent-evaporation rate, α_e . Such a dependence is summarized in a stability diagram (Figure 7) and can be verified in future experiments.

Based on these results, we are able to make an important observation about the annealing of thin BCP films by nonselective solvents. The most efficient pathway to remove the defects is to first swell the film to a sufficiently large solvent fraction where defects become unstable and then, as a second step, evaporating the solvent rapidly when the defect almost “heals” spontaneously.

We would like to conclude with a few qualitative remarks on future directions and the relation of this work to experiments. The competition between finite system size and lamellar spacing is essential in determining the dynamics of defect removal as well as the final morphology of the film. However, in this work, we have chosen only two system sizes for a given lamellar spacing. Systematic investigations of the finite-size effect should be done in the future by gradually increasing the system size to cover more periods and to unify our predictions.

The swelling dynamics of BCP films strongly depends on the BCP morphology.^{19,21} For example, films with perpendicular lamellae swell faster than parallel ones because a higher amount of the solvent can penetrate through the A/B interface that is exposed to the free surface. This effect is associated with the inhomogeneous distribution of the solvent within the microphase-separated BCP film. In our work, this is omitted because we have neglected the coupling of the swelling dynamics with BCP morphology dynamics. Nonetheless, the inhomogeneous solvent distribution and morphology-dependent swelling rate can have a significant effect on defect removal during the solvent-annealing process.

We have assumed that the relaxation dynamics throughout the film thickness is much faster than their lateral dynamics. Based on this assumption, we have neglected completely any variations of the structure and dynamics through the film thickness. However, it has been shown in many experiments^{1,3,19,21} that the structure and dynamics throughout the film thickness can be of importance during SVA processes. For example, as the solvent is introduced or removed, there must be a rearrangement of the BCP chains, and some tilting of the lamellae is expected. Moreover, the film thickness is an important parameter, used as a mean allowing a direct access to the dynamics of the structural rearrangements.^{24–26,31} By controlling the film thickness in the fully swollen state, Cavicchi et al.²⁵ found for a cylindrical BCP phase that either parallel or perpendicular orientation could be obtained. In addition, Kim and Libera²⁴ suggested that solvent diffusion toward the free surface and solvent concentration gradients within the film imposed by different solvent-evaporation rates are responsible for the different microdomains orientations.

More recently, experiments²⁶ indicated that for a swollen film of parallel cylinder morphology, when the solvent is removed instantaneously, well-ordered parallel cylinders occur. However, if the solvent is removed very slowly, the parallel cylinders reorient and become perpendicular to the substrate. Finally, it has been known that surface tension that was neglected in this work can also play some role in determining the orientation of the lamellar BCP film.^{3,31}

We believe that the insights provided in this theoretical work on defect removal from lamellar thin BCP films by SVA have the potential to greatly expand and diversify the range of applications of solvent-assisted, directed self-assembly of BCP thin films.

AUTHOR INFORMATION

Corresponding Authors

*E-mail: xu.xinpeng@gtit.edu.cn (X.X.).

*E-mail: manxk@buaa.edu.cn (X.M.).

ORCID

Xinpeng Xu: 0000-0002-3265-7678

Xingkun Man: 0000-0003-4266-1539

Notes

The authors declare no competing financial interest.

ACKNOWLEDGMENTS

We would like to thank S. Komura and T. Qian for discussions and helpful suggestions. This work was supported in part by Grant No. 21822302 and 21434001 of the National Natural Science Foundation of China (NSFC) and the joint NSFC-ISF Research Program, jointly funded by the NSFC under Grant No. 51561145002 and the Israel Science Foundation (ISF) under Grant No. 885/15. X.X. was supported by Guangdong Province Universities and Colleges Pearl River Scholar Funded Scheme (2019). D.A. acknowledges the hospitality of the ITP (CAS) and Beihang University, Beijing, China, and a CAS President International Fellowship Initiative (PIFI).

REFERENCES

- (1) Albert, J. N.; Epps, T. H., III Self-assembly of block copolymer thin films. *Mater. Today* **2010**, *13*, 24–33.
- (2) Li, W.; Müller, M. Defects in the self-assembly of block copolymers and their relevance for directed self-assembly. *Annu. Rev. Chem. Biomol. Eng.* **2015**, *6*, 187–216.
- (3) Sinturel, C.; Yayer, M.; Morris, M.; Hillmyer, M. A. Solvent vapor annealing of block polymer thin films. *Macromolecules* **2013**, *46*, 5399–5415.
- (4) Morkved, T. L.; Lu, M.; Urbas, A. M.; Ehrichs, E. E.; Jaeger, H. M.; Mansky, P.; Russell, T. P. Local control of microdomain orientation in diblock copolymer thin films with electric fields. *Science* **1996**, *273*, 931–933.
- (5) Thurn-Albrecht, T.; Schotter, J.; Kästle, G. A.; Emley, N.; Shibauchi, T.; Krusin-Elbaum, L.; Guarini, K.; Black, C. T.; Tuominen, M. T.; Russell, T. P. Ultrahigh-density nanowire arrays grown in self-assembled diblock copolymer templates. *Science* **2000**, *290*, 2126–2129.
- (6) Marencic, A. P.; Wu, M. W.; Register, R. A.; Chaikin, P. M. Orientational order in sphere-forming block copolymer thin films aligned under shear. *Macromolecules* **2007**, *40*, 7299–7305.
- (7) Shelton, C. K.; Jones, R. L.; Epps, T. H., III Kinetics of Domain Alignment in Block Polymer Thin Films during Solvent Vapor Annealing with Soft Shear: An in Situ Small-Angle Neutron Scattering Investigation. *Macromolecules* **2017**, *50*, 5367–5376.

- (8) Zhang, X.; Harris, K. D.; Wu, N. L.; Murphy, J. N.; Buriak, J. M. Fast assembly of ordered block copolymer nanostructures through microwave annealing. *ACS Nano* **2010**, *4*, 7021–7029.
- (9) Li, W.; Nealey, P. F.; de Pablo, J. J.; Müller, M. Defect removal in the course of directed self-assembly is facilitated in the vicinity of the order-disorder transition. *Phys. Rev. Lett.* **2014**, *113*, No. 168301.
- (10) Hur, S.-M.; Thapar, V.; Ramírez-Hernández, A.; Khaira, G.; Segal-Peretz, T.; Rincon-Delgado, P. A.; Li, W.; Müller, M.; Nealey, P. F.; de Pablo, J. J. Molecular pathways for defect annihilation in directed self-assembly. *Proc. Natl. Acad. Sci. USA* **2015**, *112*, 14144–14149.
- (11) Hur, S. M.; Thapar, V.; Ramírez-Hernández, A.; Nealey, P. F.; de Pablo, J. J. Defect annihilation pathways in directed assembly of lamellar block copolymer thin films. *ACS Nano* **2018**, *12*, 9974–9981.
- (12) Li, W.; Müller, M. Thermodynamics and kinetics of defect motion and annihilation in the self-assembly of lamellar diblock copolymers. *Macromolecules* **2016**, *49*, 6126.
- (13) Ren, Y.; Müller, M. Kinetics of pattern formation in symmetric diblock copolymer melts. *J. Chem. Phys.* **2018**, *148*, No. 204908.
- (14) Song, J.-Q.; Liu, Y. X.; Zhang, H. D. Removal pathways of out-of-plane defects in thin films of lamellar forming block copolymers. *Macromolecules* **2018**, *51*, 4201–4212.
- (15) Man, X.; Andelman, D.; Orland, H. Block copolymer films with free interfaces: Ordering by nanopatterned substrates. *Phys. Rev. E* **2012**, *86*, No. 010801.
- (16) Man, X.; Zhou, P.; Tang, J.; Yan, D.; Andelman, D. Defect-free perpendicular diblock copolymer films: the synergy effect of surface topography and chemistry. *Macromolecules* **2016**, *49*, 8241–8248.
- (17) Baruth, A.; Seo, M.; Lin, C. H.; Walster, K.; Shankar, A.; Hillmyer, M. A.; Leighton, C. Optimization of long-range order in solvent vapor annealed poly (styrene)-block-poly (lactide) thin films for nanolithography. *ACS Appl. Mater. Interfaces* **2014**, *6*, 13770–13781.
- (18) Zhang, J.; Posselt, D.; Sepe, A.; Shen, X.; Perlich, J.; Smilgies, D. M.; Papadakis, C. M. Structural evolution of perpendicular lamellae in diblock copolymer thin films during solvent vapor treatment investigated by grazing-incidence small-angle X-Ray scattering. *Macromol. Rapid Commun.* **2013**, *34*, 1289–1295.
- (19) Zhang, J.; Posselt, D.; Smilgies, D. M.; Perlich, J.; Kyriakos, K.; Jaksch, S.; Papadakis, C. M. Lamellar diblock copolymer thin films during solvent vapor annealing studied by GISAXS: different behavior of parallel and perpendicular lamellae. *Macromolecules* **2014**, *47*, 5711–5718.
- (20) Rudov, A. A.; Patyukova, E. S.; Neratova, I. V.; Khalatur, P. G.; Posselt, D.; Papadakis, C. M.; Potemkin, I. I. Structural changes in lamellar diblock copolymer thin films upon swelling in nonselective solvents. *Macromolecules* **2013**, *46*, 5786–5795.
- (21) Gu, X. Self-Assembly of Block Copolymers by Solvent Vapor Annealing, Mechanism and Lithographic Applications, Ph.D. Thesis, University of Massachusetts, Amherst, 2014.
- (22) Gu, X.; Gunkel, I.; Hexemer, A.; Gu, W.; Russell, T. P. An in-situ grazing incidence X-Ray scattering study of block copolymer thin films during solvent vapor annealing. *Adv. Mater.* **2014**, *26*, 273–281.
- (23) Gu, X.; Gunkel, I.; Hexemer, A.; Russell, T. P. Controlling domain spacing and grain size in cylindrical block copolymer thin films by means of thermal and solvent vapor annealing. *Macromolecules* **2016**, *49*, 3373–3381.
- (24) Kim, G.; Libera, M. Morphological development in solvent-cast polystyrene-polybutadiene-polystyrene (SBS) triblock copolymer thin films. *Macromolecules* **1998**, *31*, 2569–2577.
- (25) Cavicchi, K. A.; Russell, T. P. Solvent annealed thin films of asymmetric polyisoprene-poly(lactide) diblock copolymers. *Macromolecules* **2007**, *40*, 1181–1186.
- (26) Albert, J. N.; Young, W. S.; Lewis, R. L., III; Bogart, T. D.; Smith, J. R.; Epps, T. H., III Systematic study on the effect of solvent removal rate on the morphology of solvent vapor annealed ABA triblock copolymer thin films. *ACS Nano* **2012**, *6*, 459–466.
- (27) Paradiso, S. P.; Delaney, K. T.; García-Cervera, C. J.; Cenicerós, H. D.; Fredrickson, G. H. Block copolymer self assembly during rapid solvent evaporation: insights into cylinder growth and stability. *ACS Macro Lett.* **2013**, *3*, 16–20.
- (28) Paradiso, S. P.; Delaney, K. T.; García-Cervera, C. J.; Cenicerós, H. D.; Fredrickson, G. H. Cyclic solvent annealing improves feature orientation in block copolymer thin films. *Macromolecules* **2016**, *49*, 1743–1751.
- (29) Hur, S. M.; Khaira, G. S.; Ramírez-Hernández, A.; Müller, M.; Nealey, P. F.; de Pablo, J. J. Simulation of defect reduction in block copolymer thin films by solvent annealing. *ACS Macro Lett.* **2015**, *4*, 11–15.
- (30) Hannon, A. F.; Bai, W.; Alexander-Katz, A.; Ross, C. A. Simulation methods for solvent vapor annealing of block copolymer thin films. *Soft Matter* **2015**, *11*, 3794–3805.
- (31) Hao, J.; Wang, Z.; Wang, Z.; Yin, Y.; Jiang, R.; Li, B.; Wang, Q. Self-assembly in block copolymer thin films upon solvent evaporation: a simulation study. *Macromolecules* **2017**, *50*, 4384–4396.
- (32) Helfand, E.; Tagami, Y. Theory of the interface between immiscible polymers II. *J. Chem. Phys.* **1972**, *56*, 3592–3601.
- (33) Lodge, T. P.; Pan, C.; Jin, X.; Liu, Z.; Zhao, J.; Maurer, W. W.; Bates, F. S. Failure of the dilution approximation in block copolymer solutions. *J. Polym. Sci., Part B: Polym. Phys.* **1995**, *33*, 2289–2293.
- (34) Naughton, J. R.; Matsen, M. W. Limitations of the dilution approximation for concentrated block copolymer/solvent mixtures. *Macromolecules* **2002**, *35*, 5688–5696.
- (35) Shibayama, M.; Hashimoto, T.; Hasegawa, H.; Kawai, H. Ordered structure in block polymer solutions. 3. Concentration dependence of microdomains in nonselective solvents. *Macromolecules* **1983**, *16*, 1427–1433.
- (36) Shibayama, M.; Hashimoto, T.; Kawai, H. Ordered structure in block polymer solutions. 5. Equilibrium and nonequilibrium aspects of microdomain formation. *Macromolecules* **1983**, *16*, 1434–1443.
- (37) Huang, C. I.; Lodge, T. P. Self-consistent calculations of block copolymer solution phase behavior. *Macromolecules* **1998**, *31*, 3556–3565.
- (38) Netz, R. R.; Andelman, D.; Schick, M. Interfaces of modulated phases. *Phys. Rev. Lett.* **1997**, *79*, 1058.
- (39) Tsori, Y.; Andelman, D. Thin film diblock copolymers in electric field: transition from perpendicular to parallel lamellae. *Macromolecules* **2002**, *35*, 5161–5170.
- (40) Ciach, A.; Pekalski, J.; Gozdz, W. T. Origin of similarity of phase diagrams in amphiphilic and colloidal systems with competing interactions. *Soft Matter* **2013**, *9*, 6301–6308.
- (41) Binder, K. Phase Transitions in Polymer Blends and Block Copolymer Melts: Some Recent Developments. *Theories and Mechanism of Phase Transitions, Heterophase Polymerizations, Homopolymerization, Addition Polymerization*; Springer: Berlin, 1994; pp 181–299.
- (42) Majewski, P. W.; Yager, K. G. Rapid ordering of block copolymer thin films. *J. Phys. Condens. Matter* **2016**, *28*, No. 403002.
- (43) Brazovskii, S. A. Phase transition of an isotropic system to a nonuniform state. *J. Exp. Theor. Phys.* **1975**, *41*, 85.
- (44) Ohta, T.; Ito, A. Dynamics of phase separation in copolymer-homopolymer mixtures. *Phys. Rev. E* **1995**, *52*, 5250.
- (45) Onuki, A. Shear-induced phase separation in polymer solutions. *J. Phys. Soc. Jpn.* **1990**, *59*, 3427–3430.
- (46) Doi, M.; Onuki, A. Dynamic coupling between stress and composition in polymer solutions and blends. *J. Phys. II* **1992**, *2*, 1631–1656.
- (47) Milner, S. T. Dynamical theory of concentration fluctuations in polymer solutions under shear. *Phys. Rev. E* **1993**, *48*, 3674.
- (48) Buxton, G. A.; Clarke, N. Ordering polymer blend morphologies via solvent evaporation. *Europhys. Lett.* **2007**, *78*, S6006.
- (49) Yoo, C. D.; Viñals, J. Anisotropic linear response in block copolymer lamellar phases. *Macromolecules* **2012**, *45*, 4848–4856.
- (50) Yabunaka, S.; Ohta, T.; Yoshinaga, N. Self-propelled motion of a fluid droplet under chemical reaction. *J. Chem. Phys.* **2012**, *136*, No. 074904.

(51) Xu, X.; Thiele, U.; Qian, T. A variational approach to thin film hydrodynamics of binary mixtures. *J. Phys. Condens. Matter* **2015**, *27*, No. 085005.

(52) Yokoyama, H. Diffusion of block copolymers. *Mater. Sci. Eng., R* **2006**, *53*, 199–248.

(53) Tu, Y. O.; Drake, R. L. Heat and mass transfer during evaporation in coating formation. *J. Colloid Interface Sci.* **1990**, *135*, 562–572.

(54) Crank, J. *Free and Moving Boundary Problems*; Clarendon Press: Oxford, 1987.

(55) Liu, F.; Goldenfeld, N. Dynamics of phase separation in block copolymer melts. *Phys. Rev. A* **1989**, *39*, 4805.

(56) Müller, M.; Li, W.; Rey, J. C. O.; Welling, U. Kinetics of directed self-assembly of block copolymers on chemically patterned substrates. *J. Phys. Conf. Ser.* **2015**, *640*, No. 012010.

(57) Glotzer, S. C. Computer simulations of spinodal decomposition in polymer blends. *Annu. Rev. Comput. Phys.* **1995**, *2*, 1–46.